Ultrafast pyroelectric photodetection with on-chip spectral filters

Jon W. Stewart [1], Jarrett H. Vella[2], Wei Li [3], Shanhui Fan[3] and Maiken H. Mikkelsen [1,4]*

Thermal detectors, such as bolometric, pyroelectric and thermoelectric devices, are uniquely capable of sensing incident radiation for any electromagnetic frequency; however, the response times of practical devices are typically on the millisecond scale[1-7]. By integrating a plasmonic metasurface with an aluminium nitride pyroelectric thin film, we demonstrate spectrally selective, room-temperature pyroelectric detectors from 660–2,000 nm with an instrument-limited 1.7 ns full width at half maximum and 700 ps rise time. Heat generated from light absorption diffuses through the subwavelength absorber into the pyroelectric film producing responsivities up to 0.18 V W⁻¹ due to the temperature-dependent spontaneous polarization of the pyroelectric films. Moreover, finite-element simulations reveal the possibility of reaching a 25 ps full width at half maximum and 6 ps rise time rivalling that of semiconductor photodiodes[8]. This design approach has the potential to realize large-area, inexpensive gigahertz pyroelectric detectors for wavelength-specific detection from the ultraviolet to short-wave infrared or beyond for, for example, high-speed hyperspectral imaging.

Highly engineered infrared materials with subwavelength features have enabled an unprecedented level of control for thermal design by tailoring thermal radiation and photothermal conversion[9-14]. Thermally sensitive photodetectors leveraging these subwavelength structures, known as metamaterials, have shown fully integrated, on-chip detectors with spectrally selective responses[1-7,15] with broad wavelength sensitivities ranging from 500 nm (ref. [4]) out to 2 mm (ref. [7]). Recent work to achieve faster responses has shown picosecond internal responses through integration of a graphene bolometer with a photonic crystal[16]; however, this measurement only represents the device's pump-probe, nonlinear dynamics and not the external speed. Furthermore, the device operation hinges on the measurement of temperature-dependent noise fluctuations requiring cryogenic calibration. Several demonstrations in the 1970s achieved rise times at the nano- to picosecond scales with bulk pyroelectric crystals at room temperature[17-19]; however, these devices exhibited prohibitively low responsivities in the nV W⁻¹ to µV W⁻¹ regime and relied on intrinsic absorption features of the pyroelectric material, restricting operation to specific wavelengths and discouraging further development. Recent work with pyroelectric films has focused on leveraging pyroelectricity for hot-electron capture by using the inherent polarization of the material for charge separation. However, the large bandgap of pyroelectric materials restricts their applicability to the ultraviolet range and the fastest devices show a 53 µs response time[20,21].

Here, we experimentally and computationally demonstrate the pico- and nanosecond dynamics of a room-temperature pyroelectric photodetector that is integrated with a metallic metasurface that acts as a perfect absorber and on-chip spectral filter. The dimensions of the metasurface elements, and thus their associated plasmon resonance, solely define the detection wavelength of the detector without restrictions imposed by the bandgap of the material or intrinsic absorption features. Leveraging colloidal deposition and lithographic techniques, we demonstrate a pyroelectric detector with subnanosecond rise times and responsivities up to 180 mV W⁻¹. The detector structure consists of a film-coupled plasmonic metasurface[22] deposited on top of an aluminium nitride (AlN) pyroelectric film deposited on a p-type Si substrate as shown in Fig. 1a. Light incident on these photodetectors interacts with the resonant plasmonic metasurface giving rise to the dip in reflectance shown in Fig. 1d. At the fundamental plasmonic resonance, over 98% of the incident optical energy is converted into localized charge density oscillations confined to the metallic surfaces (that is, localized surface plasmons) between the Ag nanocube and the Au film[22]. Subsequently, the localized surface plasmons decay at femtosecond time scales and generate heat through electron–phonon scattering of the order of several picoseconds[23-26]. The generated heat then diffuses through the 75-nm-thick Au film into the underlying AlN of the order of tens of picoseconds. A simulated heat map illustrates this diffusion process in Fig. 1b,c, which shows the metamaterial unit cell 1 ps and 40 ps after excitation with a 100 fs optical pulse. Pyroelectric materials, such as AlN, possess a temperature-dependent spontaneous polarization and on heating their polarization is altered. Uniquely, pyroelectric materials exhibit increased pyroelectric coefficients when heated below their Curie temperature, which is ~2,000 °C for AlN (ref. [27]) and are thus well suited to ambient- or above-ambient-temperature operation. Sandwiching the pyroelectric material between two conductive films allows electrical charges to accumulate on the conductor–pyroelectric interfaces in an amount proportional to the polarization as shown conceptually in Fig. 1b,c. Time-varying optical/thermal signals alter the density of interfacial charges in the sandwiched structure generating a pyroelectric voltage, which drives a current i_p when connected to an external circuit as shown in equation (1), where A is the detector area, p is the pyroelectric coefficient and dT/dt is the rate of temperature change of the pyroelectric film.

$$i_p(t) = Ap\frac{\mathrm{dT}(t)}{\mathrm{dt}} \tag{1}$$

The produced time-varying pyroelectric signal is measured using a phase-sensitive electrical detection scheme using a lock-in amplifier.

¹Department of Electrical and Computer Engineering, Duke University, Durham, NC, USA. ²Sensors Directorate, Air Force Research Laboratory, Wright–Patterson Air Force Base, Dayton, OH, USA. ³Ginzton Laboratory, Department of Electrical Engineering, Stanford University, Stanford, CA, USA. ⁴Department of Physics, Duke University, Durham, NC, USA. *e-mail: m.mikkelsen@duke.edu
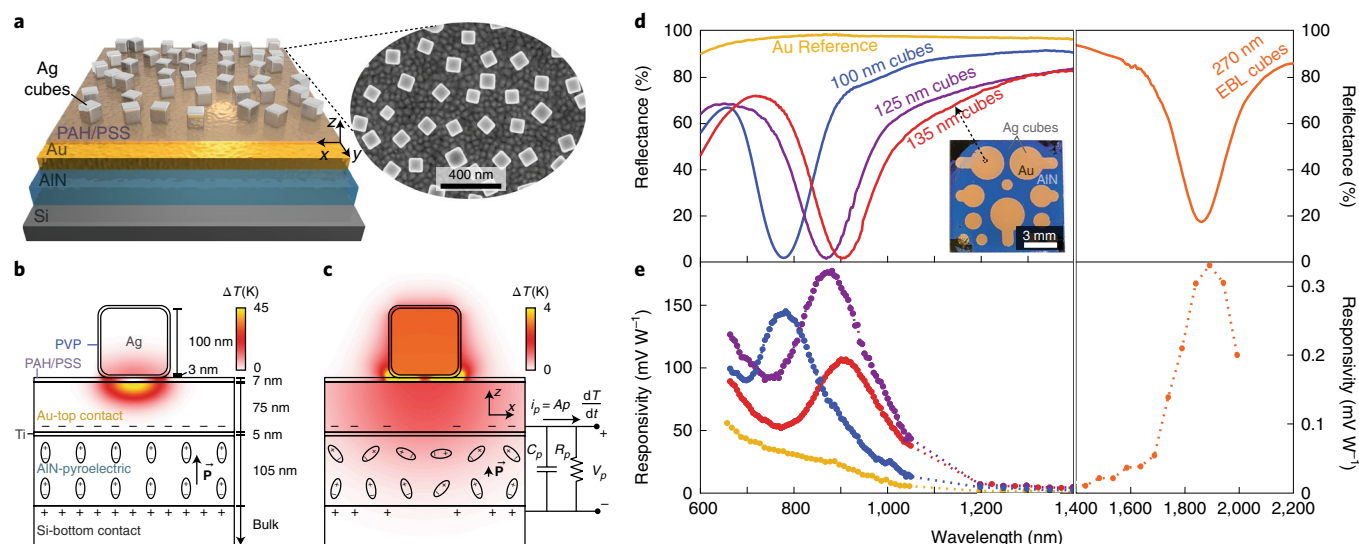
Fig. 1 | Metasurface-pyroelectric detector concept. a, Schematic of the vertical detector structure with a plasmonic metasurface deposited on a polycrystalline AlN pyroelectric layer. An SEM image of the fabricated metasurface with 100 nm Ag cubes. **b,c**, Depiction of thermal impulse response within a single metamaterial element 1 ps (**b**) and 40 ps (**c**) after an excitation pulse. The temperature change's effect on the spontaneous polarization, **P** is overlaid with the pyroelectric detection concept and the equivalent circuit of the pyroelectric film, where C_p is the capacitance, R_p the resistance, and V_p the voltage. **d**, Reflection spectra of three colloidal metasurface-pyroelectric detectors, an Au reference detector and an EBL fabricated metasurface-pyroelectric detector. Inset, an image of the 135 nm cube metasurface-pyroelectric detectors with 3.0, 2.0, 1.5 and 1.0 mm diameters. **e**, Normalized photovoltage spectra of the five different detectors showing a clear correlation with the absorption spectra. PAH, poly(allylamine) hydrochloride; PSS, polystyrene sulfonate; PVP, polyvinylpyrrolidone.

Experimentally, the colloidal metasurface-pyroelectric detectors are fabricated with two readily established techniques for both the pyroelectric films[28] and for the metasurfaces[29] capable of realizing detectors ranging from 0.0044 mm² to 7.0 mm² over wafer-scale areas. A top-down scanning electron microscope (SEM) image in Fig. 1a shows the uniformity of the self-assembled 100 nm Ag nano-cubes on an Au film. Electron-beam lithography (EBL) was used to fabricate resonances further into the infrared by interchanging the Ag nanocubes with 40-nm-thick Au nanoparticles with larger edge lengths. To characterize the spectral responsivity, five spectrally different detectors were fabricated as shown in Fig. 1d,e, where three consist of colloidal metasurfaces with varied resonances by depositing 100, 125 or 135 nm edge length cubes, one consists of 250 nm edge length Au nanoparticles patterned with EBL and the final one consists of an Au film as a control. The metasurface-pyroelectric detectors were exposed to a chopped, tunable laser and the resultant photovoltage was measured for each wavelength. Figure 1d,e shows clear agreement between the absorption spectra and responsivity, where the peak responsivities ranged between 0.11 and 0.18 V W⁻¹ for the 7.0 mm² colloidal metasurfaces and showed greater than 30 dB of selectivity between the wavelengths of fundamental resonance and 1,500 nm. The increasing responsivity of the Au control for shorter wavelengths occurs due to the interband absorption of Au, and can be reduced through the use of different plasmonic materials such as Pt, Ag and Al or mitigated through background subtraction. The EBL metasurfaces similarly show an agreement between the absorption spectrum and the spectral responsivity peaking at 0.33 mV W⁻¹ for the 1,900 nm wavelength for a 0.0072 mm² detector. By simply varying the nanoparticle size, the resonances of the metasurface-pyroelectric detectors displayed photovoltages between 660 and 2,000 nm, surpassing the spectral range of conventional InGaAs detectors.

The inherent speed of these metasurface-pyroelectric detectors was found through analysing the impulse response dynamics. Experimentally, the impulse response was measured by exciting the detectors with a 1 kHz, 100 fs laser at a wavelength of 800 nm.

Two physical mechanisms determine the ultimate speed of these detectors: the thermal time constant and the electrical time constant. The simulated temperature change, dT/dt, found with COMSOL shows a 6 ps rise time with a 25 ps full width at half maximum (FWHM), which is significantly faster than the instrument and electrical responses in the actual device. As such, the capacitance of the sandwiched pyroelectric detectors is the dominant temporal aspect, due to the slower resistance–capacitance (RC) time constant. To experimentally investigate the temporal dependence of the metasurface-pyroelectric detectors, the capacitance of the detectors was varied by fabricating detectors with diameters ranging from 75 to 1,000 μm. The impulse response for five different detector sizes is shown in Fig. 2a along with the simulated response for the 75 μm detector. For each detector size, the impulse response was fit to a single-exponential decay and the extracted time constant is plotted according to the detector area in Fig. 2b. The total RC time constant of the detector, probe and oscilloscope is also overlaid on the size dependence. The agreement between the RC time constant and the extracted exponential decay indicates that the RC time constant is indeed the dominant temporal factor for these detectors. Even with the RC-limited responses, the thermal detectors achieved response times down to a 500 ps exponential decay, a 1.67 ns FWHM and a 300 MHz bandwidth.

Computationally, finite-element simulations were used to estimate the thermal-temporal limits of the detectors. For plasmonic structures, the absorbed power density can be calculated via the conductive losses from charge oscillations induced by the plasmonic mode, which depends on the local electric field, the oscillation frequency and the imaginary permittivity[25]. In the vicinity of plasmonic nanostructures, large electric fields can produce highly localized, subwavelength absorption regions (Supplementary Fig. 2). The electromagnetic simulations were then coupled into a solid-state heat transfer simulation, where the heat source is spatially defined by the absorbed power density and temporally defined by a 100 fs FWHM Gaussian pulse. The normalized temperature maps in Fig. 1b,c were taken 1 ps and 40 ps after excitation. To account
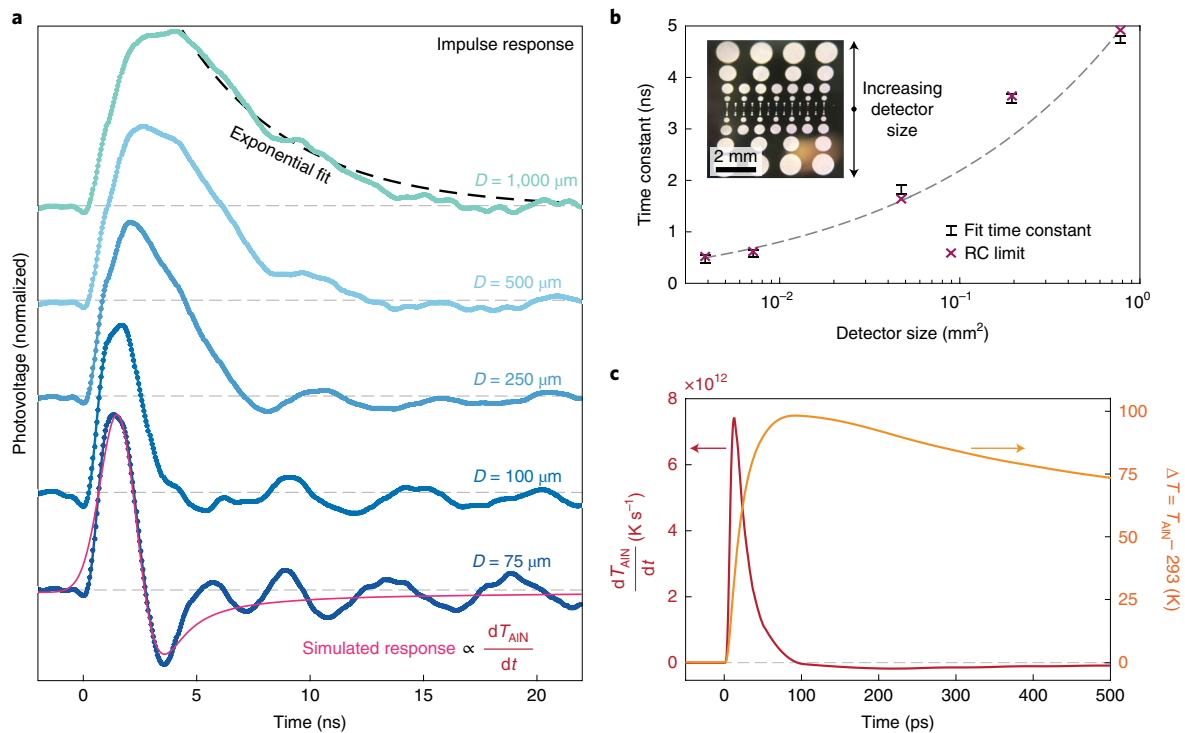
Fig. 2 | Temporal detector response. a, Photovoltage impulse response of metasurface-pyroelectric detectors after excitation with a 100 fs laser pulse at time zero (0 ns). Detectors with different diameters, D, show varying response times and are overlaid with the simulated response for the 75 μm detector convolved with its RC limit. **b,** Size-dependent exponential time constants extracted from fitting each impulse response, which are shown along with the RC-limited responses and a dashed line to guide the eye. The inset contains the fabricated metasurface-pyroelectric detectors with diameters ranging from 75 to 1,000 μm. **c,** Simulated thermal impulse response for the 75 μm detector. The rate of temperature change, dT/dt, is directly proportional to the generated pyroelectric voltage as described by equation (1).

for any size-dependent thermal relaxation, full detectors were simulated with 75–1,000 μm diameters, which showed deviations of less than 1% in their extracted lifetimes between different detector sizes. The 75 μm thermal simulation included in Fig. 2c shows a 10–90% rise time of 41 ps and a bi-exponential decay with a primary and secondary relaxation of 580 ps and 4.91 ns, respectively. To overlay the simulated and experimental results, the simulated photoresponse was calculated according to equation (1), which relates the rate of temperature change (Fig. 2c), the detector area (0.0044 mm²), the termination resistance (51.8 Ω) and the pyroelectric coefficient. The pyroelectric coefficient for AlN was extracted by fitting the magnitude of the simulation to the experimental results, which was found to be 1.9 μC cm⁻² K⁻¹ as compared to the directly measured 6–8 μC cm⁻² K⁻¹ in a previous work[30]. The discrepancy between these values probably arises from transient absorption effects during excitation by the femtosecond laser pulses, which are unaccounted for by the thermal simulations. For better visual comparison between the simulated and measured impulse responses, the simulated response was convolved with a 500 MHz Gaussian pulse corresponding to the experimental instrument-limited response time. The simulated and experimental impulse responses for the 75 μm detector (Fig. 2a) show precise temporal agreement for both the AlN depolarization and repolarization on heating and cooling following the femtosecond pulse. This agreement between the experimental and simulated results demonstrates the possibility of realizing much faster metasurface-pyroelectric detectors potentially with thermally limited 25 ps response times.

After demonstration of the picosecond-scale temporal dynamics, the detector responsivity was further characterized. Results from two different readout schemes for the pyroelectric detectors are shown in Fig. 3a, where the low-impedance readout scheme allows

for photocurrent measurements and the high-impedance readout for measuring photovoltage. Both readout schemes possess a spectral profile matching the 100 nm nanocube metasurface shown in Fig. 1d,e. The angle dependence of the same detector is depicted in Fig. 3b and it is shown that the responsivity only decreases by 7% out to 60° angles, which closely follows the metasurface angular absorption profile shown previously[29]. The power dependence was then measured to characterize the noise and sensitivity of this detector. The noise floor of the 7.0 mm² detector is depicted in Fig. 4a and shows a signal-to-noise ratio of 1 for a laser power of 1.7 μW, corresponding to an irradiance of 24 μW cm⁻². In pyroelectric/thermal detection there are multiple noise sources that determine the sensitivity of the detector, such as Johnson noise, thermal noise, 1/frequency noise and amplifier noise. In this work, Johnson noise dominates as it depends on the resistance of the detector and its temperature, which can be large for the room-temperature pyroelectric films. The 675 kΩ resistance of the 7.0 mm² detector was extracted from a current–voltage curve, as shown in Supplementary Fig. 3. The theoretical Johnson noise for this detector with a high-impedance amplifier was 106 nV Hz⁻¹/² as shown in Fig. 4b, which closely matches the mean measured noise spectral density (NSD) of 132 nV Hz⁻¹/². The low-impedance amplifier noise measurements showed better agreement between the calculated Johnson noise at 156 fA Hz⁻¹/² and the mean NSD of 162 fA Hz⁻¹/². The noise equivalent power (NEP) is calculated by dividing the NSD by the spectral responsivity. As expected, the highest NEP of 679 nW Hz⁻¹/² occurs at the highest responsivity equating to the peak metasurface absorptance as seen in Fig. 4c and can be improved by cooling the detector to decrease the Johnson noise. The specific detectivity ($D^\star$) normalizes the performance to the detector size and is calculated by dividing the area of the detector by the NEP. As such,
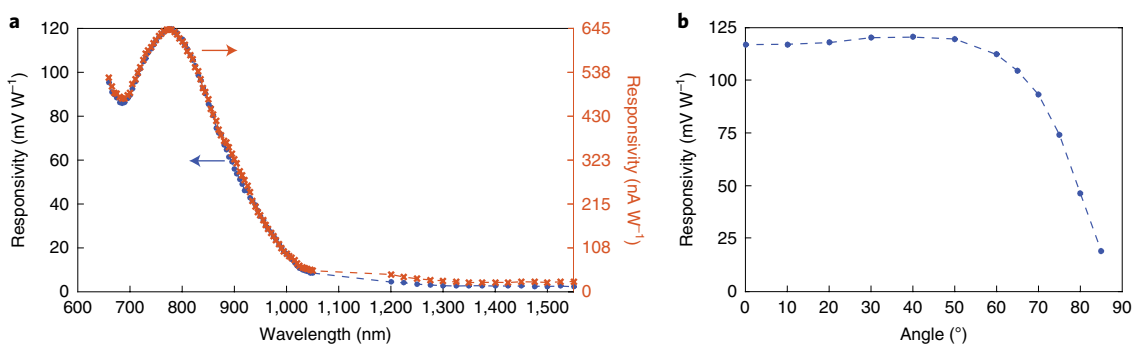
Fig. 3 | Responsivity characterization. a, Photovoltage and photocurrent responsivities of a detector fabricated with 100 nm nanocubes. **b**, The angle-dependent responsivity of the same detector showing large responsivities out to 60° angles.
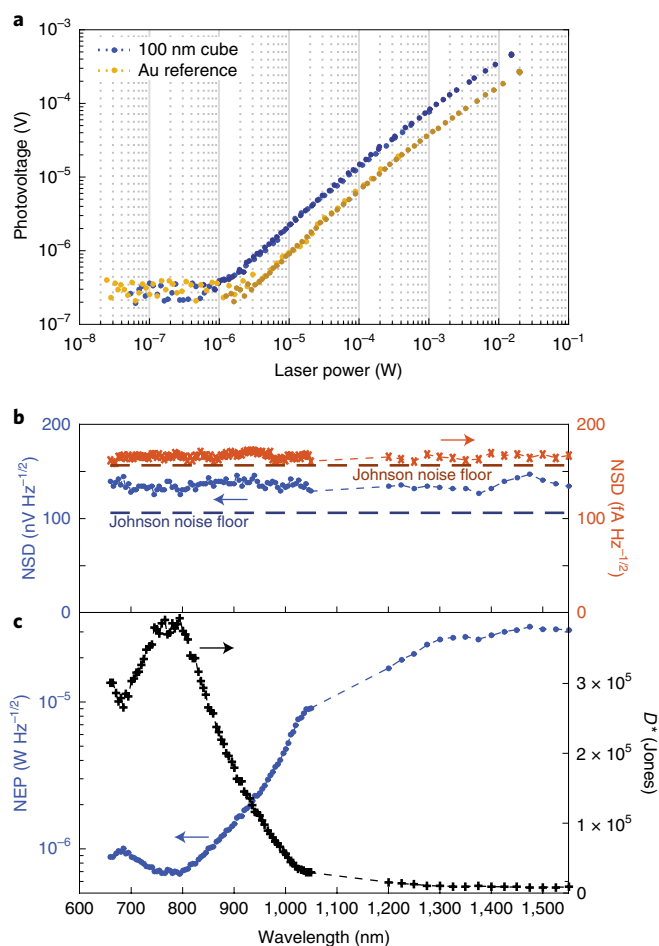

Fig. 4 | Noise performance. a, Power dependence of a detector with 100 nm cubes showing the noise floor for powers below 1 µW and a nearly linear photovoltage for increasing powers. **b**, NSD for both current and voltage measurements of the same detector. **c**, NEP calculated from the NSD showing microwatt sensitivity similar to the power-dependence noise floor plotted along with the specific detectivity (D^*).

this metasurface-pyroelectric detector shows a peak detectivity of 3.9×10^5 Jones, which can be improved using back-thinned, thermally isolated pixels, cooling the detectors or vacuum packaging of the detector.

In conclusion, a room-temperature ultrafast thermal photodetector has been demonstrated by integrating a metasurface with a

nanometre-scale pyroelectric film enabling an instrument-limited 700 ps rise time, a 1.67 ns FWHM and a 300 MHz bandwidth, which is almost six orders of magnitude faster than previously demonstrated spectrally selective thermal detectors[1–7]. Thermal transport simulations closely match the experimental results and show the potential for response times down to 25 ps for smaller detectors approaching that of semiconductor photodiodes with carrier-limited responses of ~30 ps (ref. [8]). On-chip spectral filters created by the integrated metasurfaces were used to realize spectrally selective detection from 660 to 2,000 nm. The wavelength range could be further extended into the ultraviolet–visible region through substitution of Au with Pt, Ag or Al, and into the mid-infrared by fabricating larger nanoparticles via EBL or inexpensive, large-area techniques such as deep-ultraviolet lithography or the synthesis of larger colloidal nanoparticles. These large-area devices show the potential for realizing uncooled, thermal photodetectors with high responsivities and gigahertz speeds without the spectral limitations of bandgap-based detectors. Furthermore, integrating these metasurface-pyroelectric photodetectors with multiscale patterning techniques[31] could enable on-chip hyperspectral focal plane arrays, where integration of dynamically tunable metasurfaces[32,33] could allow for spectral reconstruction with a single photodetector[34,35].

Online content

Any methods, additional references, Nature Research reporting summaries, source data, extended data, supplementary information, acknowledgements, peer review information; details of author contributions and competing interests; and statements of data and code availability are available at https://doi.org/10.1038/s41563-019-0538-6.

References

1. Dao, T. D. et al. Hole array perfect absorbers for spectrally selective midwavelength infrared pyroelectric detectors. *ACS Photon.* **3**, 1271–1278 (2016).
2. Goldsmith, J. H., Vangala, S., Hendrickson, J. R., Cleary, J. W. & Vella, J. H. Long-wave infrared selective pyroelectric detector using plasmonic near-perfect absorbers and highly oriented aluminum nitride. *J. Opt. Soc. Am. B* **34**, 1965 (2017).
3. Suen, J. Y. et al. Multifunctional metamaterial pyroelectric infrared detectors. *Optica* **4**, 276 (2017).
4. Mauser, K. W. et al. Resonant thermoelectric nanophotonics. *Nat. Nanotechnol.* **12**, 770–775 (2017).
5. Jung, J. Y. et al. Infrared broadband metasurface absorber for reducing the thermal mass of a microbolometer. *Sci. Rep.* **7**, 430 (2017).
6. Ogawa, S. & Kimata, M. Wavelength- or polarization-selective thermal infrared detectors for multi-color or polarimetric imaging using plasmonics and metamaterials. *Materials (Basel).* **10**, 493 (2017).

7. Kuznetsov, S. A., Paulish, A. G., Navarro-Ciá, M. & Arzhannikov, A. V. Selective pyroelectric detection of millimetre waves using ultra-thin metasurface absorbers. *Sci. Rep.* **6**, 1–11 (2016).
8. Gao, Y. et al. Photon-trapping microstructures enable high-speed high-efficiency silicon photodiodes. *Nat. Photon.* **11**, 301–308 (2017).
9. Raman, A. P., Anoma, M. A., Zhu, L., Rephaeli, E. & Fan, S. Passive radiative cooling below ambient air temperature under direct sunlight. *Nature* **515**, 540–544 (2014).
10. Zhai, Y. et al. Scalable-manufactured randomized glass-polymer hybrid metamaterial for daytime radiative cooling. *Science* **355**, 1062–1066 (2017).
11. Li, W., Shi, Y., Chen, Z. & Fan, S. Photonic thermal management of coloured objects. *Nat. Commun.* **9**, 4240 (2018).
12. Coppens, Z. J. & Valentine, J. G. Spatial and temporal modulation of thermal emission. *Adv. Mater.* **29**, 1701275 (2017).
13. Dongare, P. D. et al. Nanophotonics-enabled solar membrane distillation for off-grid water purification. *Proc. Natl Acad. Sci. USA* **114**, 6936–6941 (2017).
14. Biswas, R. & Povinelli, M. L. Sudden, laser-induced heating through silicon nanopatterning. *ACS Photon.* **2**, 1681–1685 (2015).
15. Dao, T. D. et al. An on-chip quad-wavelength pyroelectric sensor for spectroscopic infrared sensing. *Adv. Sci.* 1900579 https://doi.org/10.1002/advs.201900579 (2019).
16. Efetov, D. K. et al. Fast thermal relaxation in cavity-coupled graphene bolometers with a Johnson noise read-out. *Nat. Nanotechnol.* **13**, 797–801 (2018).
17. Stotlar, S. C. & McLellan, E. J. Developments in high-speed pyroelectric detectors. *Opt. Eng.* **20**, 469–471 (1981).
18. Roundy, C. B. & Byer, R. L. Subnanosecond pyroelectric detector. *Appl. Phys. Lett.* **21**, 512–515 (1972).
19. Roundy, C. B., Byer, R. L., Phillion, D. W. & Kuizenga, D. J. A 170 psec pyroelectric detector. *Opt. Commun.* **10**, 374–377 (1974).
20. Wang, Z. et al. Light-induced pyroelectric effect as an effective approach for ultrafast ultraviolet nanosensing. *Nat. Commun.* **6**, 8401 (2015).
21. Peng, W. et al. Enhanced performance of a self-powered organic/inorganic photodetector by pyro-phototronic and piezo-phototronic effects. *Adv. Mater.* **29**, 1–9 (2017).
22. Baumberg, J. J., Aizpurua, J., Mikkelsen, M. H. & Smith, D. R. Extreme nanophotonics from ultrathin metallic gaps. *Nat. Mater.* **18**, 668–678 (2019).
23. Sykes, M. E. et al. Enhanced generation and anisotropic Coulomb scattering of hot electrons in an ultra-broadband plasmonic nanopatch metasurface. *Nat. Commun.* **8**, 986 (2017).
24. Zhu, X., Vannahme, C., Højlund-Nielsen, E., Mortensen, N. A. & Kristensen, A. Plasmonic colour laser printing. *Nat. Nanotechnol.* **11**, 325–329 (2016).
25. Kong, X. T., Khosravi Khorashad, L., Wang, Z. & Govorov, A. O. Photothermal circular dichroism induced by plasmon resonances in chiral metamaterial absorbers and bolometers. *Nano Lett.* **18**, 2001–2008 (2018).
26. Spitzer, F. et al. Enhancement of electron hot spot relaxation in photoexcited plasmonic structures by thermal diffusion. *Phys. Rev. B* **94**, 201118 (2016).
27. Yan, W. S. et al. Temperature dependence of the pyroelectric coefficient and the spontaneous polarization of AlN. *Appl. Phys. Lett.* **90**, 212102 (2007).
28. Crisman, E. E., Derov, J. S., Drehman, A. J. & Gregory, O. J. Large pyroelectric response from reactively sputtered aluminum nitride thin films. *Electrochem. Solid-State Lett.* **8**, H31 (2005).
29. Akselrod, G. M. et al. Large-area metasurface perfect absorbers from visible to near-infrared. *Adv. Mater.* **27**, 8028–8034 (2015).
30. Fuflyigin, V., Salley, E., Osinsky, A. & Norris, P. Pyroelectric properties of AlN. *Appl. Phys. Lett.* **77**, 3075–3077 (2000).
31. Stewart, J. W., Akselrod, G. M., Smith, D. R. & Mikkelsen, M. H. Toward multispectral imaging with colloidal metasurface pixels. *Adv. Mater.* **29**, 1602971 (2017).
32. Hoang, T. B. & Mikkelsen, M. H. Broad electrical tuning of plasmonic nanoantennas at visible frequencies. *Appl. Phys. Lett.* **108**, 183107 (2016).
33. Peng, J. et al. Scalable electrochromic nanopixels using plasmonics. *Sci. Adv.* **5**, eaaw2205 (2019).
34. Sakoglu, U., Tyo, J. S., Hayat, M. M., Raghavan, S. & Krishna, S. Spectrally adaptive infrared photodetectors with bias-tunable quantum dots. *J. Opt. Soc. Am. B* **21**, 7–17 (2004).
35. Bao, J. & Bawendi, M. G. A colloidal quantum dot spectrometer. *Nature* **523**, 67–70 (2015).

Methods

Fabrication. Pyroelectric AlN was deposited onto 0.2-mm-thick, <111> p-type Si wafers. Substrates were heated in an ultrahigh vacuum sputtering system (base pressure 10^{-9} Torr) to 800 °C, and a 5 N Al target was radio frequency (RF) sputtered in an Ar/N_2 atmosphere. This resulted in a polycrystalline *c*-axis-orientated AlN film with a single nanometre-scale surface roughness as previously described[2,28,36]. Next, the colloidal film-coupled metasurfaces were deposited onto the AlN films through physical vapour deposition, layer-by-layer polymer deposition and finally the self-assembly of colloidally synthesized nanoparticles. In more detail, a 75 nm gold film with a 5 nm Ti adhesion layer was evaporated with an electron beam through a shadow mask onto the AlN surface. The shadow mask was used to simultaneously define the readout area of the detector as well as the metasurface area. Next, a 7 nm spacer layer was deposited using layer-by-layer dip-coating of five alternating polyelectrolyte layers composed of a positively charged poly(allylamine) hydrochloride polymer and a negatively charged polystyrene sulfonate polymer suspended in 1 M NaCl solution. Finally, the substrate was incubated in a solution of Ag nanocubes, where the nanocube stabilizer coating was ~3 nm of polyvinylpyrrolidone, a negatively charged polymer, which facilitates the nanocubes to electrostatically adhere to the positively charged polyelectrolyte layer. The Ag nanocubes were colloidally synthesized following a well-established process[37] (NanoComposix Inc.).

The high-speed metasurface-pyroelectric detectors shown in Fig. 2b were fabricated following the same procedure but without the shadow mask to pattern the Ti/Au films. After the deposition of the Ag nanocubes, a positive photoresist was spin-coated on top of the vertical detector stack and was patterned to be used as the etch mask. A noble metal etchant (Microchem GE8110) was used to etch through the Ag nanocubes and Au films. Afterwards, the AlN was etched using a $Cl_2/BCl_3/Ar$ RIE etch recipe to expose the Si substrate and isolate neighbouring detectors. The photoresist was removed with acetone and 1165 resist remover resulting in the final samples.

The EBL metasurface-pyroelectric detectors shown in Supplementary Fig. 4 were fabricated by depositing a 75 nm gold film with a 5 nm Ti adhesion layer onto the AlN film with electron-beam evaporation. The detector areas were created by patterning a positive photoresist into $85 \times 85\,\mu m^2$ squares and wet etching through the Au with GE8110 and the Ti with 10:1 buffered hydrofluoric acid. Afterwards, the AlN was etched using a $Cl_2/BCl_3/Ar$ reactive-ion etching (RIE) recipe to expose the Si substrate and isolate neighbouring detectors. A 250 nm SiO_2 film was deposited over the whole sample with plasma-enhanced chemical vapour deposition. A negative photoresist was deposited and exposed to create $75 \times 75\,\mu m^2$ wells in the resist, which were spatially aligned to the $85 \times 85\,\mu m^2$ Au/AlN pads. The exposed SiO_2 films in the wells were etched down to the Au with a CHF_3/Ar RIE etch and a 10:1 buffered hydrofluoric acid clean. This created $75 \times 75\,\mu m^2$ wells with exposed Au films and SiO_2 everywhere else on the sample. The SiO_2 film prevented the traces from shorting to the conductive Si wafer. A negative photoresist was used to pattern the Au traces to the outside of the wafer, which consisted of a 5 nm Ti and 200 nm Au film. Next, a 7 nm Al_2O_3 film was deposited with atomic layer deposition (ALD) on the entire sample except for the contact pads and the thickness was measured with ellipsometry. For the nanoparticle deposition via EBL, poly(methylmethacrylate) (PMMA) was spin-coated on the wafer and exposed with an Elionix ELS-7500 EX E-Beam Lithography System with a 2.1 µs dose at 50 pA and 50 kV. The exposed PMMA was developed and a 30 nm Au film was evaporated on the pattern. The PMMA and Au was lifted off leaving only the nanoparticles patterned on the sample. Lastly, the sample was conductive epoxied to a wafer carrier and the top traces were wire-bonded to the leads, which were connected to a female coaxial connector for readout.

Absorption measurements. The reflection spectra from 400 to 1,550 nm of the metasurface and Au detectors where measured with a custom-built microscope integrated with a visible and near-infrared spectrometer. A 50/50 beamsplitter was used to couple a broadband white light source into the microscope and spectrometer. The spectra were averaged over an area with a 60 µm diameter using a 0.15 numerical aperture objective and were normalized relative to the reflectance of an Ag mirror. The reflection spectra from 1,550 to 3,000 nm were measured on a Bruker Hyperion microscope integrated with a Vertex 80v spectrometer with a ×15 objective and were normalized relative to an Au reference.

Impulse response measurements. The impulse response of the metasurface-pyroelectric detectors was measured with a ~100 fs laser pulse generated by a Coherent Libra with a 1 kHz repetition rate at a wavelength of 800 nm. The femtosecond laser pulse can be approximated as an impulse, since the relevant dynamics of the metasurface-pyroelectric detectors were on the pico- to nanosecond time scales. The laser was attenuated through a variable neutral density (ND) filter to reduce the 3.2 W output power to 0.5–2.0 mW at the detector.

The beam was aligned into a custom-built microscope to focus the incident laser onto the various detector sizes. Electrically, a micromanipulator with a tungsten tip was used to contact the Au film and was connected to the core conductor of a coaxial cable. The shielding of the coaxial cable was bonded to the bulk p-type Si substrate, where the pyroelectric voltage was measured between the centre conductor and the shielding of the coaxial cable. The impulse response of the detectors was captured on a 1 GHz oscilloscope triggered by the external trigger of the Coherent Libra.

Responsivity measurements. A broadband SuperK supercontinuum laser with an acousto-optic tunable filter was used as a tunable monochromatic source with linewidths between 1.8 and 5.0 nm for 640–1,100 nm wavelengths and linewidths between 6.4 and 20.0 nm for the 1,200–2,000 nm wavelengths. As such, the responsivity was sampled at 5 nm intervals between 640 and 1,100 nm and 25–50 nm intervals in the 1,200–1,600 nm range to reduce the correlation between data points. Following the acousto-optic tunable filter, the laser was sent through a variable ND filter, a rotating chopper wheel and an iris, which determines the diameter of the beam. A computer-controllable flip mirror directed the laser after these optical elements to a power meter. The power meter and variable ND filter were used either for power stabilization or for the power-dependence measurements. The chopper wheel was driven with a stabilized frequency reference from a lock-in amplifier at 137 Hz. The chopped/modulated laser when absorbed by the detector produced a modulated pyroelectric voltage, enabling the lock-in amplifier to conduct phase-sensitive detection at the modulation frequency used for low-noise, high-sensitivity measurements. Before the lock-in amplifier, the signal was input into a high- or low-impedance amplifier for measuring either the photovoltage or photocurrent, respectively. The measured pyroelectric response was recorded via a Labview program for each wavelength or power step, and was divided by the laser power to get the responsivity. The NSD was provided by the lock-in amplifier to assess the noise performance of the detector.

Data availability

The data that support the findings of this study are available from the corresponding authors on reasonable request.

Code availability

The code for the optical and thermal simulations is available from the corresponding authors on reasonable request.

References

36. Iqbal, A. & Mohd-Yasin, F. Reactive sputtering of aluminum nitride (002) thin films for piezoelectric applications: A review. *Sens. (Basel)* **18**, 1797 (2018).
37. Hoang, T. B., Huang, J. & Mikkelsen, M. H. Colloidal synthesis of nanopatch antennas for applications in plasmonics and nanophotonics. *J. Vis. Exp.* **111**, e53876 (2016).

Author contributions

J.H.V. and M.H.M. conceived and planned the project. J.W.S. and J.H.V. fabricated the samples. J.W.S. built the experimental setup and performed the experiments. J.W.S. analysed the data. J.W.S. and W.L. performed the finite-element simulations. J.H.V., S.F. and M.H.M. supervised the effort. J.W.S., J.H.V. and M.H.M. wrote the manuscript. All authors discussed the results and commented on the manuscript.

Competing interests

The authors declare no competing interests.

Additional information

Supplementary information is available for this paper at https://doi.org/10.1038/s41563-019-0538-6.

Correspondence and requests for materials should be addressed to M.H.M.

Reprints and permissions information is available at www.nature.com/reprints.